Chemical Science



EDGE ARTICLE

View Article Online
View Journal | View Issue



Cite this: Chem. Sci., 2025, 16, 13944

dll publication charges for this article have been paid for by the Royal Society of Chemistry

Received 6th April 2025 Accepted 27th June 2025

DOI: 10.1039/d5sc02562a

rsc.li/chemical-science

Promoting electrocatalytic CO₂ reduction to *n*-propanol over ethanol at Cu step sites†

Yuanyuan Xue, Ximeng Lv, (1) Chao Yang, Lu Song, Lijuan Zhang* and Gengfeng Zheng (1) *

Obtaining valuable C_{3+} products directly from the electrocatalytic reduction of CO_2 or CO is an attractive but challenging task, due to the much more complicated reaction pathways and sluggish kinetics of C_{3+} products than their C_1 and C_2 counterparts. As different C_{3+} products and competitive C_2 side-products may share the common rate-determining step (e.g. the carbon-carbon coupling), the regulation of subsequent selectivity-determining step(s) is critical for promoting the selectivity of C_{3+} products. Herein, we focused on tuning the selectivity competition between n-propanol (n- C_3 H $_7$ OH, an important C_{3+} alcohol) versus ethanol (C_2 H $_5$ OH, a major C_2 side product), based on the constant potential computations on the Cu surface with different step sites. The critical selectivity-determining steps for the n- C_3 H $_7$ OH and C_2 H $_5$ OH pathways have been identified, and the impact of Cu step sites on the competitive relation between n- C_3 H $_7$ OH and C_2 H $_5$ OH has been explored. Moreover, a descriptor related closely to the n-propanol selectivity has been developed, showing that controlling the competitive hydrogenation of C_2 intermediates and C_1 - C_2 coupling processes is vital to differentiate the selectivity of n-propanol from ethanol. This work can inspire the screening and rational design of unconventional electrocatalytic sites for generating more value-added C_{3+} products from the electrocatalytic CO_2 reduction.

Introduction

The electrocatalytic CO_2 or CO reduction reaction $(CO_2RR/CORR)$ using renewable electricity has attractive potential for reducing carbon footprint and energy storage in liquid fuel products like alcohols, ¹⁻⁴ due to their high energy densities, convenient storage, and facile transportation. ^{5,6} C_1 and C_2 alcohols, *i.e.*, methanol $(CH_3OH)^{7-9}$ and ethanol (C_2H_5OH) , ¹⁰⁻¹² have relatively high selectivities and activities. In contrast, the selective electroreduction of $CO_{(2)}$ into C_{3+} alcohols, such as n-propanol (n- $C_3H_7OH)$, is still challenging versus the competing side reactions of C_1 and C_2 products. As the $CO_{(2)}$ -to- C_3H_7OH involves complicated reaction pathways containing both the C_1 - C_1 coupling and subsequent C_1 - C_2 coupling, ^{13,14} most of the reported faradaic efficiencies (FEs) of n- C_3H_7OH in $CO_{(2)}$ electroreduction are still below 20% to date. ¹⁵⁻¹⁸

A variety of approaches have been investigated to promote the selectivity of the n-propanol product from the $CO_{(2)}RR$. For instance, doping Au into Cu(100) was reported to decrease the adsorption of CO^* (where * refers to the adsorption site) while

Laboratory of Advanced Materials, State Key Laboratory of Porous Materials for Separation and Conversion, Shanghai Key Laboratory of Molecular Catalysis and Innovative Materials, Fudan University, Shanghai, 200438, China. E-mail: gfzheng@fudan.edu.cn; zhanglijuan@fudan.edu.cn

retaining the intrinsic Cu(100) active sites at the same time, which facilitated the C_1 – C_2 and C_1 – C_1 coupling process and presented a peak FE of 18% for n- C_3 H₇OH.¹⁵ Cu co-doped with Ag and Ru was synthesized for the CO electroreduction to n- C_3 H₇OH, with a 37% FE and >100 mA cm⁻² of partial current density.¹⁹ Nonetheless, the production selectivity and yield of n- C_3 H₇OH by the electrocatalytic CO₍₂₎RR are still much lower than those of the C_1 and C_2 side products and also far from the commercialization requirements.²⁰⁻²²

The selectivity of C₁ and C₂ products in the CO₍₂₎RR can be promoted based on the rate-determining step (RDS) regulation,23-29 such as using atomic structure design23 or microenvironmental tuning.24,26 However, as the C3 formation steps (e.g. the C₁-C₂ coupling and the hydrogenation of C₃ intermediates) are far away from the initial reaction stage and unlikely to serve as the RDS,30 different C3+ products and those C₂ side products may share the same RDS. Thus, it is hard to improve the selectivity of C₃₊ products by the RDS tuning strategy. The selectivities of C₃₊ products should mainly be determined by the selectivity-determining steps (SDSs) for the competitive pathways.31 Ethanol has been proposed as a major competing side product of n-C₃H₇OH.³²⁻³⁶ Wang and coworkers analyzed the reported CO2RR-relevant studies using the machine learning method and found correlation between FEs/ Δ FEs of ethanol and *n*-propanol, suggesting that ethanol and *n*propanol share the common C-C coupling process and compete

Edge Article Chemical Science

with each other.36 In addition, according to our previously reported work, the pathways to ethanol and n-propanol separate with the acetate/acetic acid pathway at an earlier stage (CH2CO*). Thus, the FE of acetate is generally low under conditions that are advantageous for the n-propanol formation.37,38 Thus, the competitive relationship between ethanol and *n*-propanol is more critical for determining the *n*-propanol selectivity in the CO₍₂₎RR. By using differential electrochemical mass spectrometry, it was found that the concentration ratios of acetaldehyde/ethanol and propionaldehyde/n-propanol near the cathode surface are higher than those in the bulk electrolyte during CO2 electroreduction, suggesting that acetaldehyde (CH₃CHO) is the bifurcation point of C₂H₅OH and n-C₃H₇OH.³² The subsequent coupling of CH₃CHO and CO* can lead to the formation of n-C₃H₇OH, while the further hydrogenation of CH₃CHO results in C₂H₅OH.³² In addition to acetaldehyde, methylcarbonyl (CH3CO*) has also been suggested as another possible branching point for the C₂H₅OH and n-C₃H₇OH pathways.34 Nonetheless, despite that they are crucial for the CO(2)RR to n-C3H7OH, the branching intermediates and selectivity-determining steps for the C₂H₅OH and n-C₃H₇OH pathways are still ambiguous, precluding the breakthrough of designing efficient electrocatalysts.

In this work, we first conducted constant potential computations to identify the selectivity-determining steps and the critical bifurcation intermediate for the n-C₃H₇OH and C₂H₅OH pathways. Then we designed a variety of high-index Cu facets with step sites and theoretically investigated for their catalytic performances on the selectivity competition between the n-C₃H₇OH and C₂H₅OH pathways. Finally, a critical descriptor was developed to predict the capabilities of different Cu sites for the CO(2)RR to n-C3H7OH, suggesting the potential of developing new electrocatalysts for more value-added products.

Results and discussion

Selectivity mechanism

As Cu(100) has been widely reported for the CO₍₂₎RR to C₂₊ products (mostly C2 products like ethylene and ethanol though),39 we first conducted constant potential calculations to explore the critical elementary steps regarding the competition between C₂H₅OH and *n*-C₃H₇OH pathways on Cu(100) (computational details in Fig. S1 and Tables S1, S2†). There are two possible bifurcation intermediates (i.e., CH₃CO* and CH₃-CHO*) for the competition pathways between C2H5OH and n-C₃H₇OH, ³²⁻³⁴ and the possible hydrogenation steps and coupling steps of those two intermediates are schematically displayed (Fig. 1a). Although CH2CHO* has also been proposed as a possible precursor to form CH₃CHO*,³⁷ the formation of CH₃CO is easier than that of CH₂CHO* (Fig. S2†). Thus, CH₃CO* is chosen as the starting point (Fig. 1a). For the hydrogenation of CH_3CO^* , the free energy change (ΔG) to CH_3CHO^* (i.e., $CH_3CO^* + H^+ + e^- \rightarrow CH_3CHO^*$) is more negative than that of CH_3COH^* (i.e., $CH_3CO^* + H^+ + e^- \rightarrow$ CH₃COH*) in the whole potential range and pH range (Fig. S3†), indicating that the carbon atom of the carbonyl group in CH₃CO* tends to obtain the proton rather than the oxygen atom

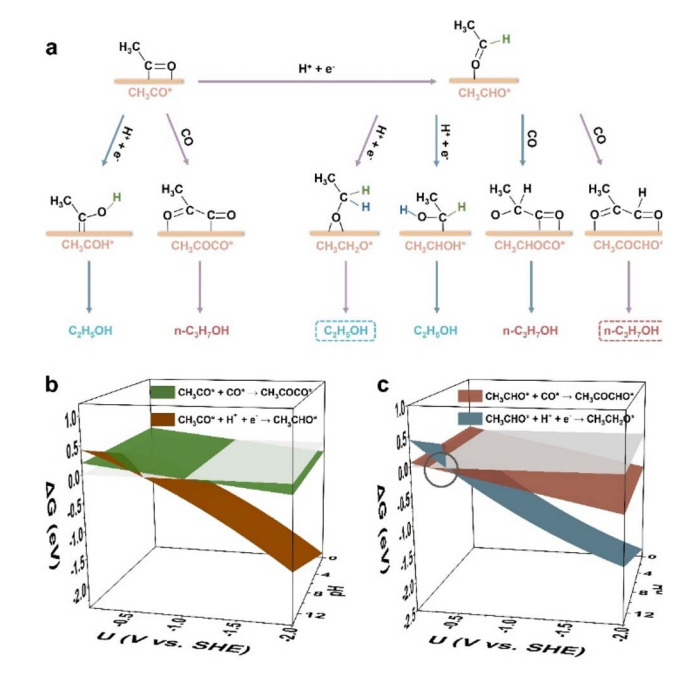


Fig. 1 (a) Possible hydrogenation and coupling steps of the two possible branching intermediates (CH3CO* and CH3CHO*) for C_2H_5OH and $n-C_3H_7OH$ pathways. The preferable hydrogenation and coupling steps of CH₃CO* and CH₃CHO* are marked with purple arrows. The hydrogen atoms from the hydrogenation of CH₃CO* are shown in green color, and the hydrogen atoms from the hydrogenation of CH₃CHO* are shown in blue color. The most possible C₂H₅OH and $n-C_3H_7OH$ pathways are highlighted with the dashed boxes. (b) Free energy changes of the hydrogenation and coupling steps of CH₃CO* on Cu(100) versus the potential and pH. (c) Free energy changes of the hydrogenation and coupling steps of CH3CHO* on Cu(100) versus the potential and pH. The circle highlights the dominant potential range (at pH 14) where the coupling step proceeds preferably. The grey planes in (b) and (c) are the planes with the function of $\Delta G = 0$ (eV).

of the carbonyl group. For the subsequent hydrogenation of CH₃CHO*, the carbon atom of the aldehyde group is also easier to obtain the proton (i.e., CH₃CH₂O*) than the oxygen atom of the aldehyde group (i.e., CH₃CHOH*) (Fig. S4†), suggesting that CH₃CH₂O* is more likely to be the key intermediate toward ethanol than CH₃CHOH*. For the *n*-propanol formation pathway (Fig. S5†), the coupling of CH₃CHO* with CO* tends to form CH₃COCHO* on Cu(100) within the whole potential and pH ranges, rather than form the CH₃CHOCO* intermediate.

From the above analysis, the most possible hydrogenation and coupling steps of CH3CO* and CH3CHO* are determined (purple arrows in Fig. 1a), among which CH₃CHO* can be obtained from the hydrogenation of CH₃CO*. As shown in Fig. 1b, the coupling between CH_3CO^* and CO^* (i.e., $CH_3CO^* + CO^* \rightarrow$ CH_3COCO^*) is preferable under alkaline conditions, as the ΔG of the CH₃CO* hydrogenation step (i.e., CH₃CO* + H⁺ + e⁻ \rightarrow CH_3CHO^*) is more positive in a higher pH environment. However, when the coupling step becomes spontaneous, ΔG of the CH₃CO* protonation step is more negative, even at pH 14. Thus, the protonation of CH₃CO* to CH₃CHO* is generally advantageous during the CO(2)RR. On the other hand, for CH₃CHO* in an alkaline environment (Fig. 1c), the coupling step (CH₃CHO* + CO* \rightarrow CH₃COCHO*) is more preferable than its protonation step in the potential range of -0.27 to -0.50 V vs. the standard hydrogen electrode (SHE) at pH 14, suggesting that CH₃CHO* is more likely to be the branching intermediate for C₂H₅OH and n-C₃H₇OH pathways. The corresponding SDS for C_2H_5OH formation is: $CH_3CHO^* + H^+ + e^- \rightarrow CH_3CH_2O^*$, and the corresponding SDS for n-C₃H₇OH formation is: CH₃-CHO* + CO* → CH₃COCHO*. Kastlunger et al. conducted microkinetic simulations based on the constant-potential density functional theory (DFT) to explore the formation of C₂ products by the CO2RR on Cu(100)40 and found that the hydrogenation of CH₃CHO* to CH₃CH₂O* led to the formation of C₂H₅OH, consistent with our results. Recently, the surface reconstruction of Cu(100) during the CO₂RR was theoretically explored by the potential-dependent grand canonical Monte Carlo method combined with the environmental kinetic Monte Carlo method and the DFT method, showing that C₂H₅OH can be produced through the hydrogenation of CH₃CHO* to CH₃-CH₂O*.41 This work also supports that the hydrogenation of CH₃CHO* is a critical step for the formation of C₂H₅OH. The free energy profiles of SDSs for both the C₂H₅OH and n-C₃H₇OH formation pathways at -0.4 V vs. SHE at pH 14 are displayed (Fig. S6†), indicating the feasibility for the $CO_{(2)}RR$ to *n*-propanol via the coupling between CH3CHO* and CO*.

When the potential becomes more negative (< $-0.50 \text{ V} \nu s$. SHE, pH 14), the hydrogenation step of *CH₃CHO toward ethanol becomes more dominant than the coupling step on Cu(100) (Fig. 1c), indicating that the perfect Cu(100) facet is hard to catalyze the CO₍₂₎RR to n-C₃H₇OH. In comparison, on Ag-doped Cu, the SDS for the n-C₃H₇OH pathway becomes dominant in the potential range between 0.22 and $-0.96 \text{ V} \nu s$. SHE at pH 14 (see ΔG (U, pH) and structures in Fig. S7, computational details in Fig. S8 and Table S3†), in accordance with the experimental observation of the enhanced n-C₃H₇OH selectivity on Ag-doped Cu, ⁴² also confirming the branching intermediate (CH₃CHO*) and SDSs for C₂H₅OH and n-C₃H₇OH pathways.

Step effects

Chemical Science

After determining the critical branching intermediate and corresponding SDSs for the C₂H₅OH and n-C₃H₇OH pathways, we further investigated the roles of surface step sites in the competition between C₂H₅OH and n-C₃H₇OH. The explicit functions of step sites on the n-C₃H₇OH selectivity were first surveyed by constructing surface steps with different upper terrace widths and lower terrace widths based on the Cu(100) facet (Fig. 2a-h). The step surfaces were constructed by removing the different numbers of atom row on the top layer of Cu(100), and the width of one row is the diameter of Cu(1.8 Å). The formed step surfaces are designated as "Step_u(x)d(y)", where "u(x)d(y)" refers to the step site unit comprising x rows at the upper terrace and y rows at the lower terrace. It was found that the adsorption of CH₃CHO* and CO* competes with each other,33 while the adsorption of CH3CHO* on Cu(100) is always weaker than that of CO* in the whole potential range of the

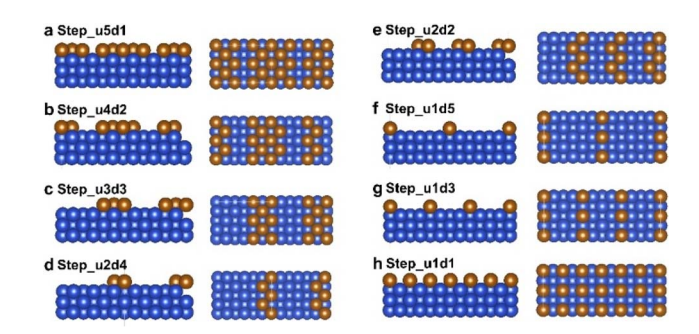


Fig. 2 (a–h) The side views and top views of different step surfaces constructed based on the Cu(100) facet, including (a) Step_u5d1, (b) Step_u4d2, (c) Step_u3d3, (d) Step_u2d4, (e) Step_u2d2, (f) Step_u1d5, (g) Step_u1d3, and (h) Step_u1d1. The Cu atoms of the uppermost layer are presented with a brown color to clearly display the step sites. These step surfaces were denoted as "Step_u(x)d(y)", which means that the upper terrace width of the step unit is "x" times the diameter of the Cu atom, and the lower terrace width of the step unit is "y" times the diameter of the Cu atom. The diameter of the Cu atom is 1.8 Å.

CO(2)RR (Fig. 3a, computational details in Fig. S9 and Table S4†). For the coupling of CH₃CHO* and CO* (i.e., the SDS for the n-propanol pathway), the adsorption of both CO* and CH_3CHO^* should be optimized. Thus, the $\Delta E_{ads}(CH_3CHO^*)$ $\Delta E_{\rm ads}({\rm CO}^*)$ ratio is used to evaluate the priority of the n-C₃H₇OH pathway, from which the ratio close to 1 suggests an optimal match of both CH₃CHO* and CO* adsorption. The ΔE_{ads} (CH₃- CHO^* / $\Delta E_{ads}(CO^*)$ ratio reaches the highest value of 0.84 when the width of the lower terrace of the Cu(100) step is 3.6 Å (Fig. 3b, computational details in Table S5†). On the other hand, for the protonation of CH_3CHO^* to $CH_3CH_2O^*$ (i.e., the SDS of the C₂H₅OH pathway), when hydrogenated CH₃CH₂O* is more stable, the possibility for the formation of C₂H₅OH increases. Thus, the $\Delta E_{\rm ads}({\rm CH_3CH_2O^*})/\Delta E_{\rm ads}({\rm CO^*})$ ratio is used to represent the protonation capability of the catalyst for C2+ intermediates, from which the smaller ratio represents that the hydrogenation step is less likely to occur. The ΔE_{ads} (CH₃CH₂- O^*)/ $\Delta E_{ads}(CO^*)$ ratio reaches the lowest value (2.45) when the width of the upper terrace is 1.8 Å (Fig. 3c, computational details in Table S5†). Based on the two indicators above, the optimal Cu(100) step is the Step_u1d2, with a lower terrace width of 3.6 Å and an upper terrace width of 1.8 Å (Fig. S10†).

To evaluate the n-C₃H₇OH selectivity of different step sites, we set the Cu(100) surface as the benchmark, and the n-C₃H₇OH relative selectivity compared to the Cu(100) surface is defined as: $(K_{\text{C}_2+\text{CO}}/K_{\text{C}_2+\text{H}} \times K_{\text{C}_3+\text{H}})$, where $K = k_{\text{step}}/k_{\text{Cu(100)}}$, k refers to the rate constant of an elementary reaction, "step" refers to the step surfaces, and "C₂ + CO", "C₂ + H", and "C₃ + H" represent the coupling of CH₃CHO* and CO* to CH₃COCHO*, the hydrogenation of CH₃CHO* to CH₃CH₂O*, and the hydrogenation of CH₃COCHO* to CH₃COCHOH* (Fig. S11†), respectively. The relative n-C₃H₇OH selectivity of the Cu(100) surface is set as 1. " $K_{\text{C}_2+\text{CO}}/K_{\text{C}_2+\text{H}}$ " represents the switching trend of the C₂H₅OH and n-C₃H₇OH pathways, which shows a linear correlation with the $\Delta E_{\text{ads}}(\text{CH}_3\text{CH}_2\text{O}^*)/\Delta E_{\text{ads}}(\text{CO}^*)$ value (Fig. 3d). Then the relative selectivity of n-C₃H₇OH on different Cu(100) steps was

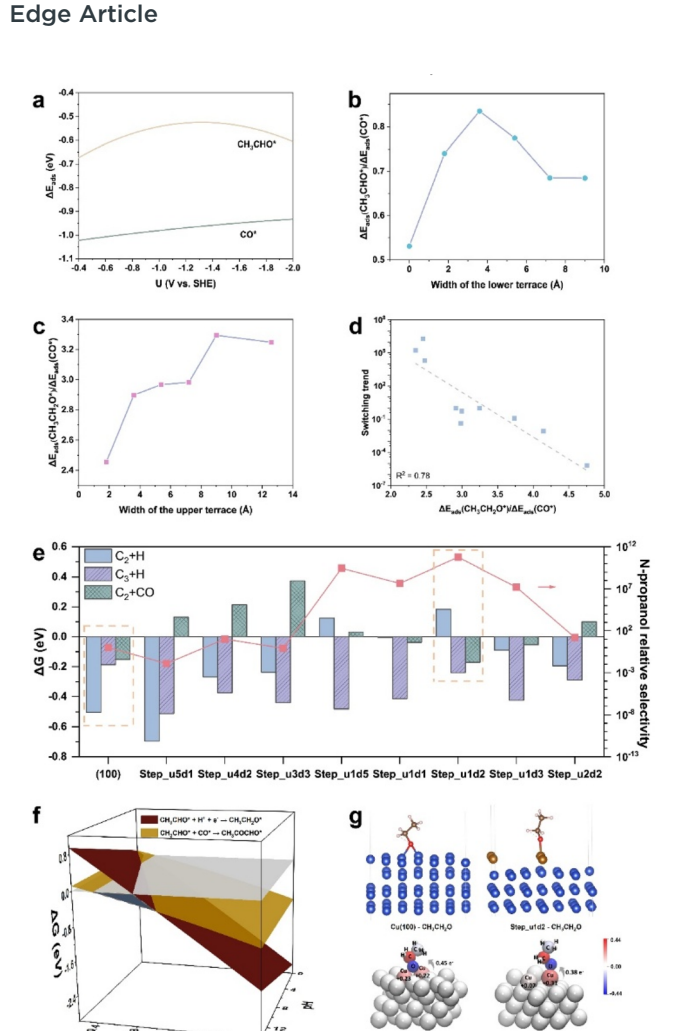


Fig. 3 (a) The adsorption energies ($\Delta E_{\rm ads}$) of CH₃CHO* and CO* on Cu(100) against the potential. (b) The adsorption energy ratios between CH3CHO* and CO* of the step surfaces constructed based on Cu(100) against the width of the lower terrace. (c) The adsorption energy ratios between CH3CH2O* and CO* of the step surfaces constructed based on Cu(100) against the width of the upper terrace. The data in (b) and (c) are from Cu(100), Step_u5d1, Step_u4d2, Step_u3d3, Step_u2d4, and Step_u1d5. (d) The relation of the switching trend (defined as K_{C_2+CO}/K_{C_2+H}) against the descriptor $\Delta E_{ads}(CH_3 CH_2O^*)/\Delta E_{ads}(CO^*)$. (e) The free energy changes of three reaction steps including the protonation of CH_3CHO^* ($C_2 + H$), the protonation of CH₃COCHO* (C₃ + H), and the coupling between CH₃CHO* and $CO*(C_2 + CO)$, and n-propanol relative selectivity of Cu(100) and step surfaces constructed based on Cu(100). (f) The free energy changes of the SDSs for n-propanol and ethanol pathways on Step_u1d2 against the potential and pH. The grey plane is the plane with the function of $\Delta G = 0$ (eV). The highlighted region with blue color shows the potential range at pH = 14 where the n-propanol is preferably produced. (g) The adsorption configurations of CH₃CH₂O* on Cu(100) and Step_u1d2 (top), and the atomic charge coloring diagrams of CH₃CH₂O* on Cu(100) and Step_u1d2 (bottom), the numbers of electron transferred from the surface adsorption sites to CH₃CH₂O* are marked.

calculated, among which the Step_u1d2 sites show the highest n-C₃H₇OH relative selectivity of 5.7 \times 10¹⁰ (Fig. 3e, right *y*-axis). The SDS of the n-C₃H₇OH pathway on Step_u1d2 is more

dominant than the ethanol pathway in the potential range of -0.41 to -1.03 V vs. SHE at pH 14 (Fig. 3f, computational details in Fig. S12 and Table S6†), wider than that of the perfect Cu(100) surface (Fig. 1c, -0.27 to -0.50 V vs. SHE). By comparing ΔG values of the hydrogenation and coupling steps of CH₃CHO* and the hydrogenation step of CH₃COCHO* on Step_u1d2 and Cu(100) (Fig. 3e, left y-axis), the suppression of the CH₃CHO* protonation contributes the most to the enhanced n-C₃H₇OH relative selectivity of Step_u1d2. The adsorption of CH3CH2O* is switched from a bridged-adsorption mode on the Cu(100) surface, to a top-adsorption mode on the Step_u1d2 sites due to the confined surface structure (Fig. 3g). This top-adsorption mode leads to the less electron transfer from Cu atoms to CH₃CH₂O* according to the Bader charge and differential charge density analysis (Fig. 3g and S13†), thus decreasing the binding strength of CH3CH2O* on Step_u1d2 (Fig. S14a, computational details in Fig. S12 and Table S6†). On the other hand, the adsorption of CH₃CHO* on Step_u1d2 is stronger than that on Cu(100) (Fig. S14b, computational details in Fig. S12 and Table S6†). The angle between the Cu-O bond (the O atom from CH₃CHO*) and the surface plane of Step_u1d2 is 64° (Fig. S15†), smaller than that of CH₃CHO* on Cu(100) (82°), indicating a geometric affinity of Step_u1d2 for the CH3CHO* adsorption. Thus, the weak adsorption of CH₃CH₂O* and the strong adsorption of CH3CHO* on Step_u1d2 together contribute to the inhibited protonation of CH3CHO* and enhanced n-C₃H₇OH relative selectivity.

Furthermore, the n-C₃H₇OH relative selectivity of Cu(100) and step sites shows a volcano trend with the ΔE_{ads} (CH₃CH₂- O^*)/ $\Delta E_{ads}(CO^*)$ value (Fig. 4a), as the adsorption energies of different reaction intermediates are correlated during the reactions.⁴³ When $\Delta E_{ads}(CH_3CH_2O^*)/\Delta E_{ads}(CO^*)$ decreases at the right side of the volcano, the hydrogenation step of CH₃-CHO* (i.e., SDS for the C2H5OH pathway) is inhibited as the adsorbed CH₃CH₂O* becomes unstable. This SDS suppression of the C2H5OH pathway is beneficial for the n-C3H7OH production. When $\Delta E_{ads}(CH_3CH_2O^*)/\Delta E_{ads}(CO^*)$ further decreases at the left side of the volcano, not only the protonation of CH₃CHO* is suppressed, but also the protonation of C₃ intermediates, like CH₃COCHO*, is also suppressed. Thus, the n-C₃H₇OH relative selectivity decreases as the ΔE_{ads} (CH₃CH₂- O^*)/ $\Delta E_{ads}(CO^*)$ further decreases (at the left side of the volcano).

Facet prediction

As the high-index facets of Cu show characteristics of different step sites, we further screened the potential facets for the electroreduction of $CO_{(2)}$ toward n- C_3H_7OH using the $\Delta E_{\rm ads}$ (CH $_3CH_2O^*$)/ $\Delta E_{\rm ads}$ (CO *) descriptor (Fig. 4b). The $\Delta E_{\rm ads}$ (CH $_3$ -CH $_2O^*$)/ $\Delta E_{\rm ads}$ (CO *) values of (433), (321), and (310) are located in the optimal range (2.0–3.0 eV). In our work, the high-index facets have been constructed from the primitive cell of Cu, to control the suitable model size for DFT computations. For instance, Cu(321) studied in this work corresponds to Cu(210) (Fig. S16 †), and a distinct experiment performance of the Cu(210) facets for the CO $_2$ RR to n-propanol was previously

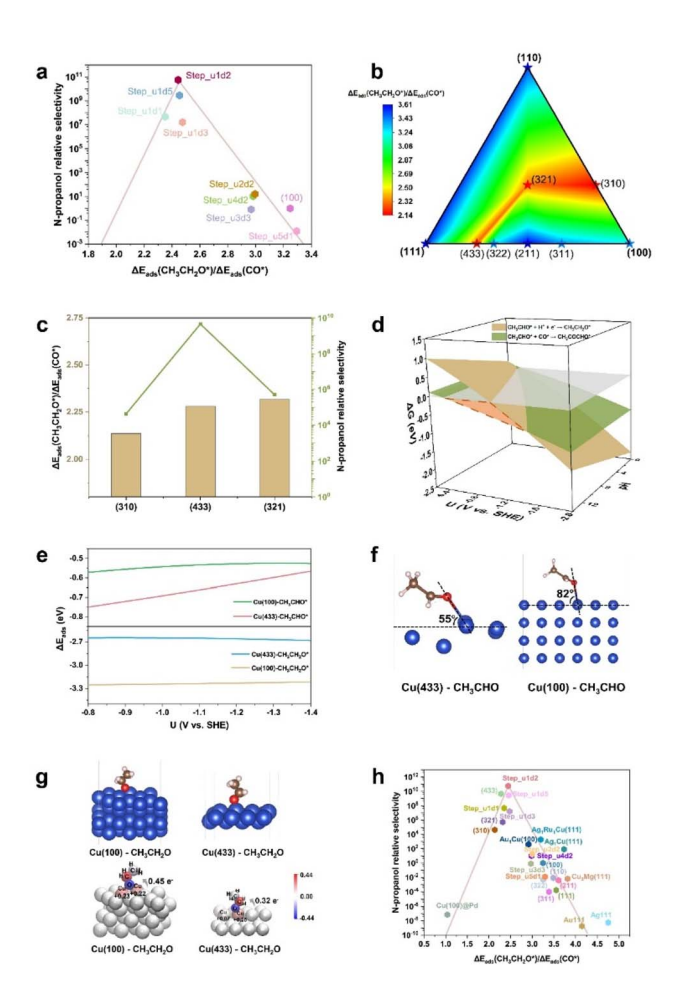


Fig. 4 (a) The volcano plot of n-propanol relative selectivity (defined as $K_{C_2+CO}/K_{C_2+H} \times K_{C_3+H}$) versus the descriptor $\Delta E_{ads}(CH_3CH_2O^*)/$ $\Delta E_{ads}(CO^*)$. (b) The contour map showing the $\Delta E_{ads}(CH_3CH_2O^*)$ / $\Delta E_{\rm ads}({\rm CO}^*)$ values of different Cu facets. (c) The n-propanol relative selectivity and $\Delta E_{\rm ads}({\rm CH_3CH_2O^*})/\Delta E_{\rm ads}({\rm CO^*})$ values of three efficient Cu facets for the $CO_{(2)}RR$ to n-propanol. (d) The free energy changes of the SDSs for n-propanol and ethanol pathways on Cu (433) against the potential and pH. The grey plane is the plane with the function of $\Delta G = 0$ (eV). The highlighted region with orange color shows the potential range at pH = 14 where the n-propanol is preferably produced. (e) The adsorption energies of CH₃CHO* (top) and CH₃-CH₂O* on Cu(100) and Cu(433) against the potential. The potential range from -0.8 to -1.4 V vs. SHE is where the formation of npropanol is preferable on Cu(433). (f) The adsorption configurations of CH₃CHO* on Cu(433) and Cu(100). The angles between the Cu-O bond and the surface are marked. (g) The adsorption configurations of CH₃CH₂O* on Cu(100) and Cu(433) (top) and the atomic charge coloring diagrams of CH₃CH₂O* on Cu(100) and Cu(433) (bottom), the numbers of electron transferred from the surface adsorption sites to $CH_3CH_2O^*$ are marked. (h) The volcano plot of the n-propanol relative selectivity versus the descriptor $\Delta E_{ads}(CH_3CH_2O^*)/\Delta E_{ads}(CO^*)$, including the data of the step surfaces (the $Step_u(x)d(y)$ surfaces and Cu facets), the Cu-based bimetals, and other metals

reported,⁴⁴ further confirming the practicability of the selectivity descriptor.

Compared to different facets, Cu(433) exhibits the highest relative selectivity ($\sim 10^9$) of *n*-propanol (Fig. 4c). The potential range for *n*-propanol production on Cu(433) was calculated to

be -0.40 to -1.49 V vs. SHE at pH 14 (Fig. 4d, computational details in Fig. S17 and Table S7†), which covers the experimentally observed potential range (-1.20 to -1.50 V vs. SHE, at pH 14) for n-propanol production, 15,20 further indicating the great potential of Cu(433) in the CO₍₂₎RR to n-propanol. Compared to Cu(100), Cu(433) shows a stronger adsorption for CH₃CHO* and a weaker adsorption for CH₃CH₂O* in the potential range for n-propanol production (Fig. 4e, computational details in Fig. S17 and Table S7†). Thus, the hydrogenation of CH₃CHO* on Cu(433) becomes difficult and the ethanol pathway is inhibited. The strong adsorption of CH₃CHO* on Cu(433) is attributed to the geometric effect from the step sites. Compared to Cu(100), CH₃CHO* adsorbed on Cu(433) is closer to the surface (Fig. 4f), allowing a strong interaction between the CH₃CHO* and the Cu(433) surface. On the other hand, CH₃-CH₂O* is adsorbed at the bridged-sites on Cu(100), and at the top-sites on Cu(433) (Fig. 4g). The less electron transfer from Cu(433) to the adsorbed CH₃CH₂O* results in the weak adsorption of CH3CH2O* based on the Bader charge and differential charge density analysis (Fig. 4g and S18†).

To more clearly show the practicability of the selectivity descriptor $\Delta E_{\rm ads}(CH_3CH_2O^*)/\Delta E_{\rm ads}(CO^*)$, the experimentally reported Cu(321) facet was compared with the Cu(100) and Cu(433) facets. As shown in Fig. S19,† the high n-propanol relative selectivity of Cu(321) is also mainly from its capability for inhibiting the hydrogenation of CH₃CHO*. The binding strength of Cu(321) for CH₃CHO* is stronger than that of Cu(100) and weaker than that of Cu(433) (Fig. S20†). The adsorption configuration of CH₃CHO* adsorbed on Cu(321) was analyzed (Fig. S21†). The angle between the Cu-O bond and the surface plane is smaller than that of Cu(100) (82°) and larger than that of Cu(433) (55°), suggesting that the capability of Cu(321) to stabilize the CH₃CHO* intermediate is superior to that of Cu(100) and inferior to that of Cu(433). On the other hand, the adsorption of CH₃CH₂O* on Cu(321) is weaker than that on Cu(100) and stronger than that on Cu(433) (Fig. S22†). Furthermore, CH₃CH₂O* is also adsorbed on Cu(321) in a topadsorption way, and the charge transfer of Cu(321) to the CH₃CH₂O* intermediate is less than that of Cu(100) and more than that of Cu(433) (Fig. S23†), confirming that the capability of Cu(321) to adsorb CH₃CH₂O* is between that of Cu(100) and Cu(433). Therefore, the *n*-propanol relative selectivity of Cu(321)is higher than that of Cu(100) and lower than that of Cu(433) (Fig. 4c). On Cu(321), the preferable potential range (at pH 14) for the coupling of CH_3CHO^* with CO^* is 0 to -0.75 V vs. SHE according to the constant potential calculations (Fig. S24, computational details in Fig. S25, and Table S8†). The overall selectivities of Cu(100), Cu(321), and Cu(433) for *n*-propanol were further calculated by considering the mainly competitive carbon-containing products (methane, methanol, ethylene, and ethanol) in the $CO_{(2)}RR$ to *n*-propanol (Fig. S26†). Cu(100) was also used as a reference in those calculations. The *n*-propanol overall selectivities (by considering all the possible carboncontaining products) on Cu(433) and Cu(321) are calculated to be $\sim 10^9$ and $\sim 10^6$, respectively (Fig. S27†), which are close to the *n*-propanol relative selectivities of the two facets (Fig. 4c). This result confirms that the n-propanol relative selectivity is

a reasonable metric to evaluate the *n*-propanol selectivity of different structures.

Finally, the relative selectivities of n-propanol of all step surfaces (including the step surfaces based on Cu(100) and different Cu facets), the Cu-based bimetals (structures in Fig. S28†), and other metals (structures in Fig. S29†), with respect to the descriptor $\Delta E_{\rm ads}({\rm CH_3CH_2O^*})/\Delta E_{\rm ads}({\rm CO^*})$, exhibit a volcano correlation (Fig. 4h). This result suggests that the selectivity descriptor $\Delta E_{\rm ads}({\rm CH_3CH_2O^*})/\Delta E_{\rm ads}({\rm CO^*})$ is universal in finding the various catalysts for the $CO_{(2)}RR$ to *n*-propanol. The Step_u1d2 sites and Cu(433) are located at the top of the volcano plot, suggesting that the capability of those surface Cu catalytic sites toward higher CO₍₂₎-to-n-propanol conversion selectivities. Although the step surfaces may experience reconstruction during the CO(2)RR due to the high surface energies and the harsh reaction conditions, there have been some reports those have successfully synthesized the high-index Cubased facets and retained good reaction stability.44-46 For example, by utilizing OH anions as the controlling reagents and the ascorbic acid for the slow growth of the nanocrystals, the Cu₂O(211) facets were synthesized, showing a FE_{C.H.} of 87% in the CO₂RR after being stored in 1 M KOH for one month. ⁴⁵ In addition, it has been found that the presence of the low-index facets can help to stabilize the high-index facets under electroreduction conditions.46 Those studies can inspire the synthesis of high-index Cu-based facets for the CO(2)RR catalysis.

Conclusions

Edge Article

In summary, this work represents a rational theoretical design for the electrocatalytic sites for efficient $CO_{(2)}$ -to- C_{3+} products based on the constant potential computations. For the formation of n-propanol, ethanol shares the common RDS and is a main side product. In our work, CH_3CHO^* has been identified as the critical intermediate for the bifurcation of n-propanol and ethanol pathways, and $\Delta E_{\rm ads}(CH_3CH_2O^*)/\Delta E_{\rm ads}(CO^*)$ has been proposed as a key descriptor for the formation of n-propanol. Based on this descriptor, different step sites have been screened to select the optimal catalytic sites, and Cu(433) facets have been suggested as the most promising facets for the electrochemical $CO_{(2)}$ -to-n-propanol conversion. Our work highlights the significance of SDS regulation in the $CO_{(2)}$ RR and allows understanding the competition mechanism between the C_2 and C_{3+} products.

Data availability

All data supporting this work are included in the ESI.†

Author contributions

Y. Xue and G. Zheng designed the research. L. Zhang and G. Zheng supervised the research. Y. Xue, X. Lv, C. Yang, and L. Song performed the research and analyzed the data. Y. Xue and G. Zheng wrote the manuscript. All the authors discussed, commented on and revised the manuscript.

Conflicts of interest

There are no conflicts to declare.

Acknowledgements

We thank the following funding agencies for supporting this work: the National Key Research and Development Program of China (2024YFB4106400 and 2024YFB4106401), the National Natural Science Foundation of China (22025502, U23A20552, and 22379026), and the Natural Science Foundation of Shanghai (23ZR1407000). The computations in this research were performed using the CFFF platform of Fudan University.

Notes and references

- A. Shayesteh Zeraati, F. Li, T. Alkayyali, R. Dorakhan,
 E. Shirzadi, F. Arabyarmohammadi, C. P. O'Brien,
 C. M. Gabardo, J. Kong, A. Ozden, M. Zargartalebi, Y. Zhao,
 L. Fan, P. Papangelakis, D. Kim, S. Park, R. K. Miao,
 J. P. Edwards, D. Young, A. H. Ip, E. H. Sargent and
 D. Sinton, Nat. Synth., 2025, 4, 75-83.
- 2 Y. Ji, Z. Chen, R. Wei, C. Yang, Y. Wang, J. Xu, H. Zhang, A. Guan, J. Chen, T.-K. Sham, J. Luo, Y. Yang, X. Xu and G. Zheng, *Nat. Catal.*, 2022, 5, 251–258.
- 3 K. Qi, Y. Zhang, N. Onofrio, E. Petit, X. Cui, J. Ma, J. Fan, H. Wu, W. Wang, J. Li, J. Liu, Y. Zhang, Y. Wang, G. Jia, J. Wu, L. Lajaunie, C. Salameh and D. Voiry, *Nat. Catal.*, 2023, **6**, 319–331.
- 4 X. He, L. Lin, X. Li, M. Zhu, Q. Zhang, S. Xie, B. Mei, F. Sun, Z. Jiang, J. Cheng and Y. Wang, *Nat. Commun.*, 2024, 15, 9923.
- 5 C. F. Shih, T. Zhang, J. Li and C. Bai, *Joule*, 2018, 2, 1925–1949.
- 6 J. M. Spurgeon and B. Kumar, Energy Environ. Sci., 2018, 11, 1536–1551.
- 7 S. Kong, X. Lv, X. Wang, Z. Liu, Z. Li, B. Jia, D. Sun, C. Yang, L. Liu, A. Guan, J. Wang, G. Zheng and F. Huang, *Nat. Catal.*, 2023, **6**, 6–15.
- 8 J. Zhang, P. Yu, C. Peng, X. Lv, Z. Liu, T. Cheng and G. Zheng, *ACS Catal.*, 2023, 13, 7170–7177.
- 9 Y. Xin, C. B. Musgrave III, J. Su, J. Li, P. Xiong, M. Meng-Jung Li, Y. Song, Q. Gu, Q. Zhang, Y. Liu, W. Guo, L. Cheng, X. Tan, Q. Jiang, C. Xia, B. Zhong Tang, W. A. Goddard III and R. Ye, *Angew. Chem., Int. Ed.*, 2025, **64**, 202420286.
- 10 Z. Liu, L. Song, X. Lv, M. Liu, Q. Wen, L. Qian, H. Wang, M. Wang, Q. Han and G. Zheng, J. Am. Chem. Soc., 2024, 146, 14260-14266.
- 11 C. Peng, J. Ma, G. Luo, S. Yan, J. Zhang, Y. Chen, N. Chen, Z. Wang, W. Wei, T.-K. Sham, Y. Zheng, M. Kuang and G. Zheng, Angew. Chem., Int. Ed., 2024, 63, 202316907.
- 12 C. Peng, S. Yang, G. Luo, S. Yan, M. Shakouri, J. Zhang, Y. Chen, Z. Wang, W. Wei, T.-K. Sham and G. Zheng, Small, 2023, 19, 2207374.
- 13 M. Sun and B. Huang, Adv. Energy Mater., 2024, 14, 2400152.

14 T. Yan, X. Chen, L. Kumari, J. Lin, M. Li, Q. Fan, H. Chi, T. J. Meyer, S. Zhang and X. Ma, *Chem. Rev.*, 2023, 123, 10530-10583.

Chemical Science

- 15 S. Jeong, C. Huang, Z. Levell, R. X. Skalla, W. Hong, N. J. Escorcia, Y. Losovyj, B. Zhu, A. N. Butrum-Griffith, Y. Liu, C. W. Li, D. Reifsnyder Hickey, Y. Liu and X. Ye, J. Am. Chem. Soc., 2024, 146, 4508–4520.
- 16 N. Sakamoto, K. Sekizawa, S. Shirai, T. Nonaka, T. Arai, S. Sato and T. Morikawa, *Nat. Catal.*, 2024, 7, 574–584.
- 17 C. Peng, G. Luo, J. Zhang, M. Chen, Z. Wang, T.-K. Sham, L. Zhang, Y. Li and G. Zheng, *Nat. Commun.*, 2021, **12**, 1580.
- 18 B. Yang, L. Chen, S. Xue, H. Sun, K. Feng, Y. Chen, X. Zhang, L. Xiao, Y. Qin, J. Zhong, Z. Deng, Y. Jiao and Y. Peng, *Nat. Commun.*, 2022, 13, 5122.
- 19 X. Wang, P. Ou, A. Ozden, S.-F. Hung, J. Tam, C. M. Gabardo, J. Y. Howe, J. Sisler, K. Bertens, F. P. García de Arquer, R. K. Miao, C. P. O'Brien, Z. Wang, J. Abed, A. S. Rasouli, M. Sun, A. H. Ip, D. Sinton and E. H. Sargent, *Nat. Energy*, 2022, 7, 170–176.
- 20 W. Niu, Z. Chen, W. Guo, W. Mao, Y. Liu, Y. Guo, J. Chen, R. Huang, L. Kang, Y. Ma, Q. Yan, J. Ye, C. Cui, L. Zhang, P. Wang, X. Xu and B. Zhang, *Nat. Commun.*, 2023, 14, 4882.
- 21 J. Li, F. Che, Y. Pang, C. Zou, J. Y. Howe, T. Burdyny, J. P. Edwards, Y. Wang, F. Li, Z. Wang, P. De Luna, C. T. Dinh, T. T. Zhuang, M. I. Saidaminov, S. Cheng, T. Wu, Y. Z. Finfrock, L. Ma, S. H. Hsieh, Y. S. Liu, G. A. Botton, W. F. Pong, X. Du, J. Guo, T. K. Sham, E. H. Sargent and D. Sinton, Nat. Commun., 2018, 9, 4614.
- 22 Y. Pang, J. Li, Z. Wang, C.-S. Tan, P.-L. Hsieh, T.-T. Zhuang, Z.-Q. Liang, C. Zou, X. Wang, P. De Luna, J. P. Edwards, Y. Xu, F. Li, C.-T. Dinh, M. Zhong, Y. Lou, D. Wu, L.-J. Chen, E. H. Sargent and D. Sinton, *Nat. Catal.*, 2019, 2, 251–258.
- 23 S. Yan, Z. Chen, Y. Chen, C. Peng, X. Ma, X. Lv, Z. Qiu, Y. Yang, Y. Yang, M. Kuang, X. Xu and G. Zheng, J. Am. Chem. Soc., 2023, 145, 26374–26382.
- 24 Z. Liu, X. Lv, S. Kong, M. Liu, K. Liu, J. Zhang, B. Wu, Q. Zhang, Y. Tang, L. Qian, L. Zhang and G. Zheng, *Angew. Chem.*, *Int. Ed.*, 2023, 62, 202309319.
- 25 M. Kuang and G. Zheng, Chem Catal., 2023, 3, 100565.
- 26 L. Yang, X. Lv, C. Peng, S. Kong, F. Huang, Y. Tang, L. Zhang and G. Zheng, *ACS Cent. Sci.*, 2023, **9**, 1905–1912.
- 27 Y. Xue, L. Zhang, M. Kuang and G. Zheng, *ACS Appl. Mater.*, 2025, **17**, 11375–11388.
- 28 Y. Jiang, L. Huang, C. Chen, Y. Zheng and S.-Z. Qiao, *Energy Environ. Sci.*, 2025, **18**, 2025–2049.

- 29 Z. Zhang, W. Gee, P. Sautet and A. N. Alexandrova, *J. Am. Chem. Soc.*, 2024, **146**, 16119–16127.
- 30 K. S. Exner, ACS Catal., 2020, 10, 12607-12617.
- 31 C. Lucky, S. Jiang, C.-R. Shih, V. M. Zavala and M. Schreier, Nat. Catal., 2024, 7, 1021–1031.
- 32 E. L. Clark and A. T. Bell, *J. Am. Chem. Soc.*, 2018, **140**, 7012–7020.
- 33 A. H. M. da Silva, Q. Lenne, R. E. Vos and M. T. M. Koper, *ACS Catal.*, 2023, **13**, 4339–4347.
- 34 X. Chang, A. Malkani, X. Yang and B. Xu, *J. Am. Chem. Soc.*, 2020, **142**, 2975–2983.
- 35 J. Li, C. Li, J. Hou, W. Gao, X. Chang, Q. Lu and B. Xu, *J. Am. Chem. Soc.*, 2022, **144**, 20495–20506.
- 36 X. He, Y. Su, J. Zhu, N. Fang, Y. Chen, H. Liu, D. Zhou and C. Wang, *J. Mater. Chem. A*, 2023, **11**, 18106–18114.
- 37 Q. Li, J. Wu, C. Yang, S. Li, C. Long, Z. Zhuang, Q. Li, Z. Guo, X. Huang and Z. Tang, J. Am. Chem. Soc., 2025, 147, 6688– 6697.
- 38 R. Zhang, J. Zhang, S. Wang, Z. Tan, Y. Yang, Y. Song, M. Li, Y. Zhao, H. Wang and B. Han, *Angew. Chem., Int. Ed.*, 2024, 63, 202405733.
- 39 G. L. De Gregorio, T. Burdyny, A. Loiudice, P. Iyengar, W. A. Smith and R. Buonsanti, ACS Catal., 2020, 10, 4854– 4862.
- 40 G. Kastlunger, H. H. Heenen and N. Govindarajan, *ACS Catal.*, 2023, **13**, 5062–5072.
- 41 S. Zhang, Q. Tang, B. Zhu and Y. Gao, ACS Catal., 2025, 15, 6497–6506.
- 42 X. Wang, Z. Wang, T.-T. Zhuang, C.-T. Dinh, J. Li, D.-H. Nam, F. Li, C.-W. Huang, C.-S. Tan, Z. Chen, M. Chi, C. M. Gabardo, A. Seifitokaldani, P. Todorović, A. Proppe, Y. Pang, A. R. Kirmani, Y. Wang, A. H. Ip, L. J. Richter, B. Scheffel, A. Xu, S.-C. Lo, S. O. Kelley, D. Sinton and E. H. Sargent, *Nat. Commun.*, 2019, 10, 5186.
- 43 M. M. Montemore and J. W. Medlin, *Catal. Sci. Technol.*, 2014, 4, 3748–3761.
- 44 D. Zhong, Z.-J. Zhao, Q. Zhao, D. Cheng, B. Liu, G. Zhang, W. Deng, H. Dong, L. Zhang, J. Li, J. Li and J. Gong, *Angew. Chem.*, *Int. Ed.*, 2021, **60**, 4879–4885.
- 45 A. M. Harzandi, S. P. Amouzesh, J. Xu, T. Baghban-Ronaghi, S. Shadman, F. Collins, G. Kim, W. Kaminsky, L. A. Curtiss and C. Liu, *Appl. Catal.*, B, 2025, 366, 125053.
- 46 J. Zhang, X. Xu, L. Luo, T. Peng, B. Liu, L. Jiang, M. Jin, R. Wang, H. Yi and W. Wu, *Chem. Eng. J.*, 2025, **503**, 158187.